PNAS RESEARCH ARTICLE | IMMUNOLOGY AND INFLAMMATION

Phosphorylation of DNA-PKcs at the S2056 cluster ensures efficient and productive lymphocyte development in XLF-deficient mice

Yimeng Zhu[a], Wenxia Jiang[a], Brian J. Lee[a], Angelina Li[b], Steven Gershik[a], and Shan Zha[a,c,d,e,1]

Edited by Sue Jinks-Robertson, Duke University School of Medicine, Durham, NC; received December 26, 2022; accepted April 20, 2023

The nonhomologous end-joining (NHEJ) pathway is a major DNA double-strand break repair pathway in mammals and is essential for lymphocyte development. Ku70 and Ku80 heterodimer (KU) initiates NHEJ, thereby recruiting and activating the catalytic subunit of DNA-dependent protein kinase (DNA-PKcs). While DNA-PKcs deletion only moderately impairs end-ligation, the expression of kinase-dead DNA-PKcs completely abrogates NHEJ. Active DNA-PK phosphorylates DNA-PKcs at two clusters—PQR around S2056 (S2053 in mouse) and ABCDE around T2609. Alanine substitution at the S2056 cluster moderately compromises end-ligation on plasmid-based assays. But, mice carrying alanine substitution at all five serine residues within the S2056 cluster (*DNA-PKcs*$^{PQR/PQR}$) display no defect in lymphocyte development, leaving the physiological significance of S2056 cluster phosphorylation elusive. Xlf is a nonessential NHEJ factor. *Xlf*$^{-/-}$ mice have substantial peripheral lymphocytes that are completely abolished by the loss of DNA-PKcs, the related ATM kinases, other chromatin-associated DNA damage response factors (e.g., 53BP1, MDC1, H2AX, and MRI), or RAG2-C-terminal regions, suggesting functional redundancy. While ATM inhibition does not further compromise end-ligation, here we show that in XLF-deficient background, DNA-PKcs S2056 cluster phosphorylation is critical for normal lymphocyte development. Chromosomal V(D)J recombination from *DNA-PKcs*$^{PQR/PQR}$*Xlf*$^{-/-}$ B cells is efficient but often has large deletions that jeopardize lymphocyte development. Class-switch recombination junctions from *DNA-PKcs*$^{PQR/PQR}$*Xlf*$^{-/-}$ mice are less efficient and the residual junctions display decreased fidelity and increased deletion. These findings establish a role for DNA-PKcs S2056 cluster phosphorylation in physiological chromosomal NHEJ, implying that S2056 cluster phosphorylation contributes to the synergy between XLF and DNA-PKcs in end-ligation.

DNA-PKcs | S2056 phosphorylation | nonhomologous end-joining | V(D)J recombination | class-switch recombination

Significance

The S2056 (PQR) cluster is one of the two autophosphorylation clusters on DNA-PKcs. Despite extensive structural and biochemical characterization, the physiological significance of S2056 cluster phosphorylation on chromosomal nonhomologous end-joining (NHEJ) remains elusive in part due to the lack of measurable phenotype in the alanine substitution mouse models. Using the Xlf-deficient background, our study documents a physiological role for the PQR cluster phosphorylation in the end-ligation step of chromosomal NHEJ and suggests an overlapping role between PQR site autophosphorylation and Xlf-mediated end-ligation.

DNA double-strand breaks (DSBs) are the most severe form of DNA damage. The nonhomologous end-joining (NHEJ) pathway is one of the two major DSB repair pathways (1–3). In mammals, NHEJ entails two processes, the conserved end-ligation, and the relatively vertebrate-specific end-processing, both depending on Ku70–Ku80 (KU) heterodimer. KU initiates NHEJ by encircling the double-stranded DNA ends and recruiting the conserved LIG4–XRCC4–XLF–PAXX complex for end-ligation (4–7). DNA-bound KU also recruits and activates the large catalytic subunit of DNA-dependent protein kinase (DNA-PKcs). Together, KU and DNA-PKcs form the DNA-PK holoenzyme, which recruits and activates Artemis endonuclease for end-processing, including the hairpin opening. In mouse models, loss of DNA-PKcs has a moderate effect on direct ligation of compatible ends but abrogates end-processing by Artemis endonuclease (4, 5, 8).

In addition to general DSB repair, NHEJ is exclusively required for V(D)J recombination that assembles the functional T cell and B cell receptor genes during lymphocyte development. Thus, NHEJ-deficient patients and mouse models often display severe immunodeficiency (5–7, 9). Briefly, RAG initiates V(D)J recombination and generates two blunt signal ends (SEs) and two covalently sealed hairpinned coding ends (CEs). In the following reaction phase, the two SEs are directly and precisely joined via NHEJ to form a signal join (SJ). At the same time, the two CEs are opened via DNA-PKcs and Artemis before being ligated together to form a coding join (CJ). Thus, *DNA-PKcs*$^{-/-}$ lymphocytes form SJs efficiently while accumulating hairpinned CEs, while Lig4-deficient cells completely fail to form either CJs or SJs and accumulate both CEs and SEs (10). The CJ encodes the variable region exon of B and T cell receptor genes that are required for

Author contributions: Y.Z. and S.Z. designed research; Y.Z., W.J., B.J.L., A.L., S.G., and S.Z. performed research; Y.Z., B.J.L., and S.Z. contributed new reagents/analytic tools; Y.Z., and S.Z. analyzed data; W.J. supported mouse genetic works; and Y.Z. and S.Z. wrote the paper.

The authors declare no competing interest.

This article is a PNAS Direct Submission.

[1]To whom correspondence may be addressed. Email: sz2296@cumc.columbia.edu.

This article contains supporting information online at https://www.pnas.org/lookup/suppl/doi:10.1073/pnas.2221894120/-/DCSupplemental.

Published June 12, 2023.

further lymphocyte development. As a result, both functional B and T lymphocytes are absent in DNA-PKcs null or Lig4-deficient mice.

Upon exposure to antigens, with the help of T cells, naïve B cells undergo additional gene rearrangement, namely the immunoglobulin heavy chain (IgH) class-switch recombination (CSR), to achieve different effector functions. CSR replaces the initially expressed Cμ constant region exons (encoding IgM antibody) with a set of downstream constant region exons encoding different antibody isotypes (e.g., Cγ1 for IgG1). CSR can be mediated by both the NHEJ pathway and the alternative end-joining (Alt-EJ) pathway that preferentially uses microhomology (MH) at the junctions. Loss of Xrcc4, Lig4, or Xlf causes a 50 to 75% decrease in CSR with the residual CSR mediated by the Alt-EJ pathway (10–15). Consistent with end-processing not being absolutely required for CSR, DNA-PKcs-null B cells have at most ~10% reduction of IgG1 CSR and a mild accumulation of unrepaired IgH breaks that can only be detected with sensitive IgH FISH (16, 17). Using high-throughput genome-wide translocation sequencing (HTGTS) (18) that allows the analysis of thousands of CSR junctions from a single bait site at Sμ, we showed that the residual CSR junctions recovered from the DNA-PKcs-null cells show a significant skew toward MHs, thus the Alt-EJ pathway (19), suggesting a role of DNA-PKcs in the end-ligation phase of NHEJ beyond previously appreciated (see below). In addition, chromosomal V(D)J recombination and CSR also activate the DNA damage response (DDR) orchestrated by the ataxia telangiectasia mutated (ATM) kinase. Correspondingly, loss of ATM and one of its chromatin-bound substrates (e.g., H2AX, 53BP1) also has a significant and synergistic impact on V(D)J recombination and CSR with NHEJ deficiency (20–22). In particular, ATM inhibition or deletion abolishes residual SJ formation and CSR in DNA-PKcs-null cells, indicating functional interaction between ATM and DNA-PKcs (23–25). Analyses of V(D)J and CSR efficiency and junctions provide valuable information on the regulation of physiological chromosomal NHEJ.

How does DNA-PKcs promote NHEJ? Single-molecule studies suggest that DNA-PKcs might have a synapsis function to promote accurate end-ligation (26, 27) by forming a dimer between the two DNA ends. A recent cryo-EM study provides visual evidence for the long-range complex between two DNA ends formed by DNA-PKcs and XLF that binds to the KU on each side of the break (28). In recent years, several studies have suggested a previously less appreciated role of DNA-PKcs in end-ligation. In contrast to the normal development of *DNA-PKcs*$^{-/-}$ mice, *DNA-PKcs*$^{KD/KD}$ mice expressing a catalytically inactive form of DNA-PKcs die during embryonic development with complete end-ligation defects. *DNA-PKcs*$^{KD/KD}$ cells can open hairpin CEs efficiently but cannot form either CJ or SJ during chromosomal V(D)J recombination assays (29). Cryo-EM analyses also showed that the Apo form of DNA-PK embraces and blocks the dsDNA end (30). In this context, DNA-PKcs is the best-characterized substrate of DNA-PK and is phosphorylated in at least two major clusters, the PQR cluster around S2056 (S2053 in mouse) and the ABCDE cluster flanking T2069. Ectopically expressed DNA-PKcs with alanine substitution at both PQR and ABCDE clusters (referred to as 7A) fail to restore IR resistance or episomal end-ligation in DNA-PKcs-null cells (31), suggesting a role of autophosphorylation on NHEJ. Loss of either ABCDE or PQR cluster phosphorylation moderately compromises end-ligation on plasmid substrates (31). To determine the physiological impact of DNA-PKcs autophosphorylation, we and others generated mouse models with knock-in alanine substitutions at either the PQR (*DNA-PKcs*^{PQR}) or ABCDE (*DNA-PKcs*^{3A} and *DNA-PKcs*^{5A}) cluster (*SI Appendix*, Fig. S1*A*) (32–34). While the *DNA-PKcs*$^{5A/5A}$ and *DNA-PKcs*$^{3A/3A}$ mice and cells show, at most, mild defects in V(D)J recombination and CSR that are exacerbated by inhibiting ATM kinase, *DNA-PKcs*$^{PQR/PQR}$ mice show no measurable defects in V(D)J recombination (33). *DNA-PKcs*$^{PQR/PQR}$ mice also carry out efficient CSR with no change in MH usage or resection. Collectively, these results suggest that end-blocking by kinase-dead DNA-PKcs cannot be attributed to the either autophosphorylation cluster alone. It also leaves the physiological function of PQR site phosphorylation in chromosomal NHEJ undetermined (33). While deletion or inhibition of ATM, a protein kinase with an overlapping substrate pool with DNA-PKcs, abolished end-ligation in DNA-PKcs-null cells (24, 25, 35), ATM kinase inhibitor did not affect chromosomal V(D)J recombination or CSR in *DNA-PKcs*$^{PQR/PQR}$ B cells (33), suggesting that the lack of end-ligation defects in *DNA-PKcs*$^{PQR/PQR}$ mice cannot be explained by compensatory phosphorylation by ATM. Correspondingly, the PQR mutation does not abolish DNA damage–induced DNA-PK kinase activity (33).

The XRCC4-like factor (XLF) is a nonessential NHEJ factor that is not required for the end-ligation of chromosomal SJs, or CJs. Xlf null mice have substantial peripheral lymphocytes (14) that are completely abolished by the loss of ATM kinase and its related chromatin-bound DDR factors (e.g., 53BP1, MDC1, MRI, H2AX, or RAG2 C-terminal domain), suggesting functional redundancy (22, 36–40). Moreover, loss of Xlf exacerbates the end-ligation defects in other NHEJ partially deficient mice—including both PAXX null (41–47) and DNA-PKcs-null mice (48), leading to neonatal lethality and abrogating chromosomal V(D)J recombination. To test whether the presence of Xlf masks the role of DNA-PKcs PQR phosphorylation on chromosomal NHEJ, we generated *DNA-PKcs*$^{PQR/PQR}$*Xlf*$^{-/-}$ mice. In contrast to single-deficient mice, *DNA-PKcs*$^{PQR/PQR}$*Xlf*$^{-/-}$ mice display severe lymphocytopenia consistent with V(D)J recombination defects. HTGTS of chromosomal V(D)J recombination junctions reveals markedly increased end-resection, large deletions, and severely reduced SJ fidelity to less than 10%. CSR to IgG1 is also further decreased in *DNA-PKcs*$^{PQR/PQR}$*Xlf*$^{-/-}$ cells than that in the *Xlf*$^{-/-}$ control. Taken together, our study provides physiological evidence for the role of PQR cluster phosphorylation in chromosomal NHEJ. The distinct synergy between ATM inhibition and ABCDE cluster phosphorylation (49) vs. those between XLF deficiency and PQR cluster phosphorylation reported here further suggests a potentially different function of PQR vs. ABCDE cluster phosphorylation of DNA-PKcs.

Results

***DNA-PKcs*$^{PQR/PQR}$*Xlf*$^{-/-}$ Mice Display Severe Lymphocytopenia.** *DNA-PKcs*$^{PQR/PQR}$*Xlf*$^{-/-}$ mice were born at the expected ratio and of normal size (*SI Appendix*, Fig. S1 *B* and *C*). Given the embryonic lethality of *Lig4*$^{-/-}$ mice, this result suggests that, at most, only a subset of NHEJ is blocked in the *DNA-PKcs*$^{PQR/PQR}$*Xlf*$^{-/-}$ mice. But in contrast to *DNA-PKcs*$^{PQR/PQR}$ or *Xlf*$^{-/-}$ mice, *DNA-PKcs*$^{PQR/PQR}$*Xlf*$^{-/-}$ mice display severe and isolated lymphocytopenia that is not associated with changes in HSPCs, nor in erythroid or megakaryocyte lineages (Fig. 1 *A–D* and *SI Appendix*, Fig. S1 *D–J*). Specifically, flow cytometry analyses show that *DNA-PKcs*$^{PQR/PQR}$*Xlf*$^{-/-}$ mice have a severe reduction of the naïve (B220^{mid}IgM^{+}) and recirculating B (B220^{high}IgM^{+}) and T (CD4^{+}CD8^{-} and CD4^{-}CD8^{+} single positive, SP) lymphocytes in major lymphoid organs (Fig. 1 *B–D*). The ratio of pre-B cells that successfully completed IgH V(D)J recombination vs. that of pro-B cells that are undergoing IgH rearrangement is significantly lower in the bone marrow of *DNA-PKcs*$^{PQR/PQR}$*Xlf*$^{-/-}$ mice (Fig. 1*E*), consistent

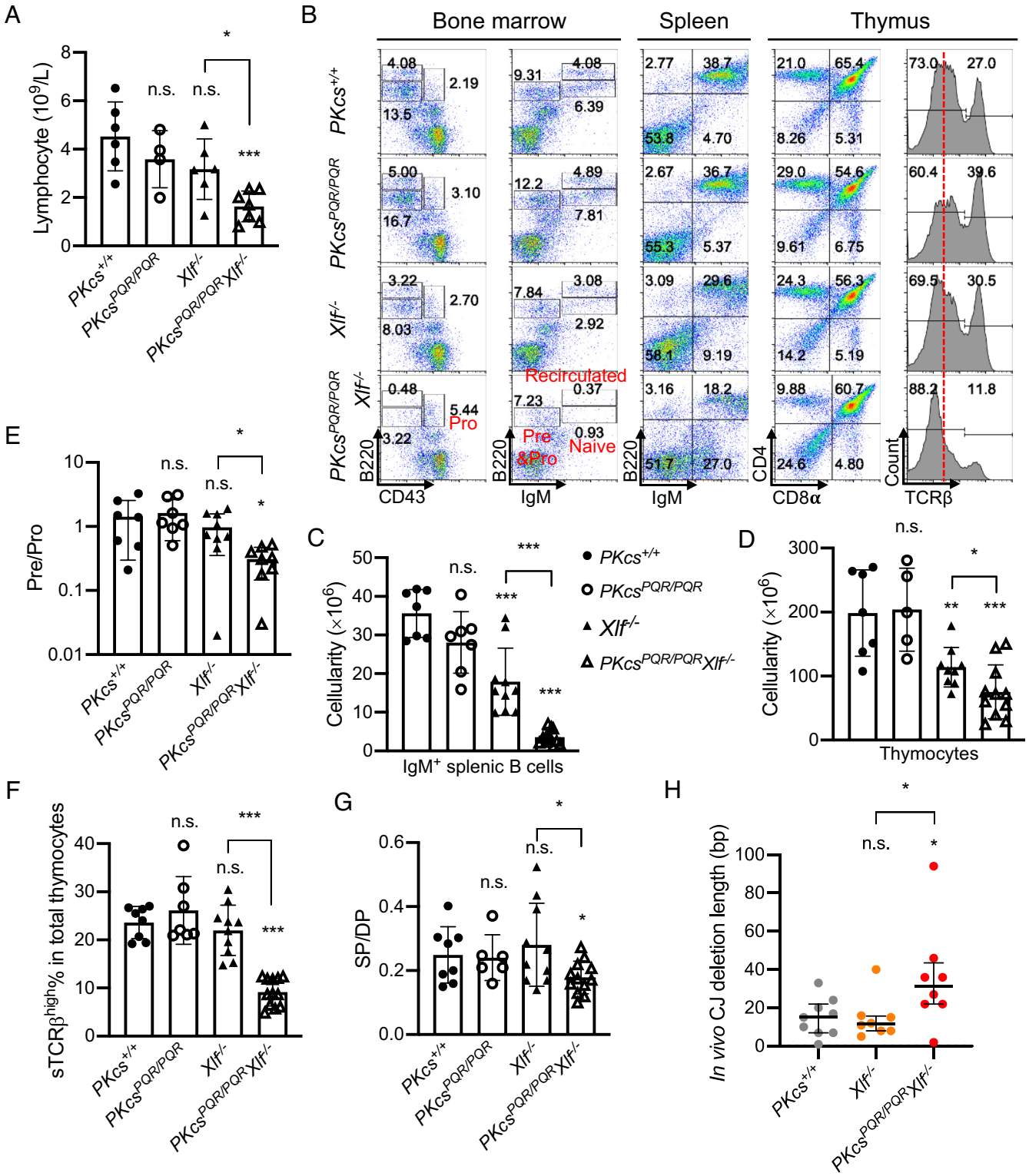

Fig. 1. S2056 cluster phosphorylation is important for early lymphocyte development in *Xlf*$^{-/-}$ mice. (*A*) Absolute lymphocyte count concentration (10^9/L) in peripheral blood of indicated mice. (*B*) Representative flow cytometric analyses of the bone marrow, spleen, and thymus from *DNA-PKcs*$^{+/+}$, *DNA-PKcs*$^{PQR/PQR}$, *Xlf*$^{-/-}$, and *DNA-PKcs*$^{PQR/PQR}$*Xlf*$^{-/-}$ mice. Numbers on the plot are percentages of cells among the gated populations. (*C* and *D*) The total IgM$^+$ splenic B cell numbers (*C*) and total thymocyte numbers (*D*). (*E*) The ratio of pre-B (B220^{mid}IgM$^-$CD43$^-$) versus pro-B (B220$^+$IgM$^-$CD43$^+$) cells in the bone marrow. (*F*) Frequency of surface-TCRβ^{high} (the right peak in panel *B*) cells in the thymus. (*G*) The ratio between the sum of CD4$^+$ or CD8$^+$ single-positive T cells (SP) and CD4$^+$CD8$^+$ double-positive (DP) immature T cells in the thymus from mice of different genotypes. (*H*) The deletion length (bp) of endogenous DQ52 to JH4 CJ in IgH locus from bone marrow cells was plotted (n = 8 or 9). Deletions from both sides of the break were added together. The lines indicate median with interquartile range. Mann–Whitney test was used to calculate the *P* value. For panels *A* and *C*–*G*, the average ± SD from at least four mice of each genotype was plotted. Student's *t* test was used to calculate the *P* value. n.s., no significant difference. *$P < 0.05$, **$P < 0.01$, ***$P < 0.001$.

with V(D)J recombination defects. Similarly, the frequency of surface TCRβ^{high} thymocytes (Fig. 1*F*) and the SP vs. CD4$^+$CD8$^+$ double-positive (DP) ratio (Fig. 1*G*), two measurements for successful V(D)J recombination at the TCRα locus in developing T cells, are also markedly decreased in *DNA-PKcs*$^{PQR/PQR}$*Xlf*$^{-/-}$ mice. Sequence analyses of the V(D)J recombination junctions in bone marrow cells

(IgH) and thymic cells (TCRβ) derived from mice show longer CJ and SJ deletion and less SJ fidelity (22.6% vs. 48.3%) in *DNA-PKcs*$^{PQR/PQR}$*Xlf*$^{-/-}$ cells than in *Xlf*$^{-/-}$ cells (Fig. 1*H* and *SI Appendix*, Fig. S1*K* and Table S1). Taken together, these data suggest that in Xlf-deficient background, loss of DNA-PKcs PQR cluster phosphorylation abrogates lymphocyte development in a way that is consistent with V(D)J recombination defects.

***DNA-PKcs*$^{PQR/PQR}$*Xlf*$^{-/-}$ Cells Support Substantial Chromosomal V(D)J Recombination.** To characterize the chromosomal V(D)J recombination defects in *DNA-PKcs*$^{PQR/PQR}$*Xlf*$^{-/-}$ lymphocytes, we generated v-abl kinase–transformed B cells from control wild-type, *DNA-PKcs*$^{PQR/PQR}$, *Xlf*$^{-/-}$, and *DNA-PKcs*$^{PQR/PQR}$*Xlf*$^{-/-}$ mice that carried Bcl-2 transgenes (22, 29, 45, 50). Treatment of v-abl-transformed pro-B cells with STI571/Gleevec, a v-abl tyrosine kinase inhibitor, arrests cells in G1 and induces RAG recombinase expression, resulting in efficient V(D)J recombination of integrated substrates (e.g., pMX-INV) in wild-type cells (50). The Bcl-2 transgene is necessary to obviate the apoptotic effects of STI571 (50). Multiple v-abl B cell lines from each genotype were generated, and each harbor a chromosomally integrated inverted V(D)J recombination substrate (pMX-INV) designed to assay both CJs and unjoined CEs (Fig. 2*A*). To do those experiments, DNA from individual lines was prepared on day 0 (before treatment), and on day 2, and day 4 after STI571 treatment, digested with restriction enzymes, and southern blotted with the appropriate probe (Fig. 2*B*). Correct rearrangement will lead to the inversion of the GFP and the formation of a 5′ SJ and a 3′ CJ (50) (Fig. 2*A*). The GFP will be in the same transcriptional orientation as the LTR promoter, leading to GFP expression (*SI Appendix*, Fig. S2). Wild-type and *DNA-PKcs*$^{PQR/PQR}$ lines generated substantial CJs and GFP expression after 2 and 4 d of STI treatment with little or no obvious free CEs (Fig. 2*B* and *SI Appendix*, Fig. S2). In contrast, as previously reported, *Xrcc4*$^{-/-}$ and *DNA-PKcs*$^{-/-}$ lines accumulated high levels of free CEs, indicative of a severe NHEJ defect (Fig. 2*B* and *SI Appendix*, Fig. S2). *Xlf*$^{-/-}$ lines generated substantial levels of CJs and GFP, but also a modest level of unjoined CEs at days 2 and 4 (Fig. 2*B* and *SI Appendix*, Fig. S2). *DNA-PKcs*$^{PQR/PQR}$*Xlf*$^{-/-}$ lines, especially clone 2, had lower levels of CJs and GFP expression at day 2, then seemed to catch up at day 4 to levels comparable to that of the *Xlf*$^{-/-}$ control (Fig. 2*B* and *SI Appendix*, Fig. S2). The result suggests that loss of DNA-PKcs PQR phosphorylation moderately attenuated remaining chromosomal V(D)J recombination in *Xlf*$^{-/-}$ cells. But the level of CEs and percentage of successful rearrangements at day 4 after induction in the *DNA-PKcs*$^{PQR/PQR}$*Xlf*$^{-/-}$ cells seem insufficient to explain the severe developmental defects in *DNA-PKcs*$^{PQR/PQR}$*Xlf*$^{-/-}$ mice vs. the *Xlf*$^{-/-}$ controls (Fig. 1*B*). We considered two possibilities. For one, the developing lymphocytes might not have the "extra time" available to Bcl2-expressing v-abl B cells to make the delayed joining in vivo. While RAG2-deficient pro-B cells that cannot initiate V(D)J recombination accumulate in vivo, NHEJ-deficient pro-B cells with unrepaired breaks at the IgH loci never accumulate, suggesting rapid elimination of pro-B cells with unrepaired breaks (22, 39, 51). Alternatively, given the deletion we saw in the endogenous IgH and TCR loci (Fig. 1*H* and *SI Appendix*, Fig. S1*K* and Table S1), we consider that large deletions might jeopardize lymphocyte development in vivo by removing the short D elements.

***DNA-PKcs*$^{PQR/PQR}$*Xlf*$^{-/-}$ Cells Have Increased Deletion at CJ of Chromosomal V(D)J Recombination.** To understand whether the quality of the CJ formed in *DNA-PKcs*$^{PQR/PQR}$*Xlf*$^{-/-}$ cells might explain the severe lymphocyte development defects in *DNA-PKcs*$^{PQR/PQR}$*Xlf*$^{-/-}$ mice in comparison to the *Xlf*$^{-/-}$ controls, we performed HTGTS (18, 52) (*SI Appendix*, Fig. S3). In these experiments, we placed the bait primer at either a CE (Fig. 3) or an SE (Fig. 4). The results revealed thousands of individual joins formed between the bait break site and a different genome-wide joining partner (the prey) (*SI Appendix*, Fig. S3). In addition to sequence information, HTGTS can also reveal the orientation of the joining product. We defined the junction in the 5′ to 3′ direction as plus (in blue) and the 3′ to 5′ orientation relative to the substrate as minus (in red). In both WT and *DNA-PKcs*$^{PQR/PQR}$ lines, the vast majority (~75%) of the preys for the 5′CEs bait are the canonical 3′CEs (in plus orientation—blue), indicative of faithful CJs on the V(D)J recombination substrate (Fig. 3 *A* and *B*). Wild-type and *DNA-PKcs*$^{PQR/PQR}$ cells have minimal levels of hybrid joins (HJs) (2 to 4%) that represent mis-joining between the 5′CE and 5′SE (Fig. 3 *A* and *B*). *Xlf*$^{-/-}$ lines accumulated a higher frequency of HJ (11.85%). In the *DNA-PKcs*$^{PQR/PQR}$*Xlf*$^{-/-}$ lines, about 25% of the junctions were HJs, leading to a corresponding decrease of the canonical CJs (down to 62% from 77%) (Fig. 3*B*). CJ formation requires the opening of the CE

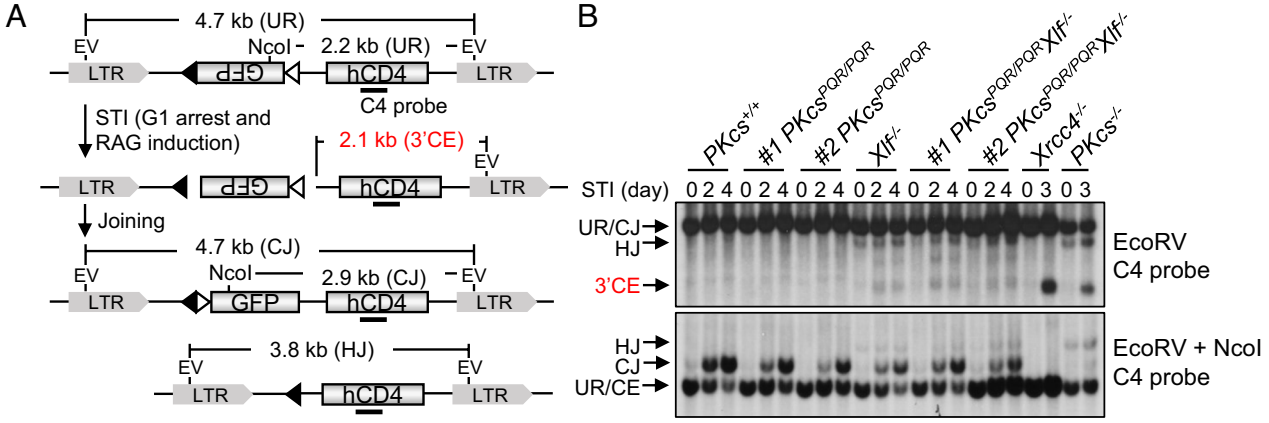

Fig. 2. DNA-PKcs S2056 cluster phosphorylation has minor impact on chromosomal V(D)J recombination efficiency. (*A*) Schematic of pMX-INV chromosomal V(D)J recombination substrates. The pMX-INV vector has a major pair of recombination signal sequences (RSSs) flanking the inverted GFP cassette. LTR = long terminal repeat from the retrovirus vector, hCD4 = truncated hCD4 cDNA encoding the transmembrane and extracellular domains of human CD4, IRES = Internal ribosome entry sites (between GFP and hCD4), filled triangle = 5′ 12-spacer RSS, open triangle = 3′ 23-spacer RSS, and EV = EcoRV cutting site. The diagram includes unrearranged substrate (UR), coding end (CE) intermediates, 4.7 kb coding joint (CJ), and 3.8 kb hybrid joints (HJ) products. Canonical V(D)J recombination between 12 and 23 RSSs inverts the GFP cassette and forms a signal joint (SJ) and a CJ. (*B*) Southern blot of EcoRV-digested (*Top*) or EcoRV-NcoI-double-digested (*Bottom*) DNA with the C4 probe. The genotypes and the days of STI treatment were marked on the top. The identities of the products were marked on the left.

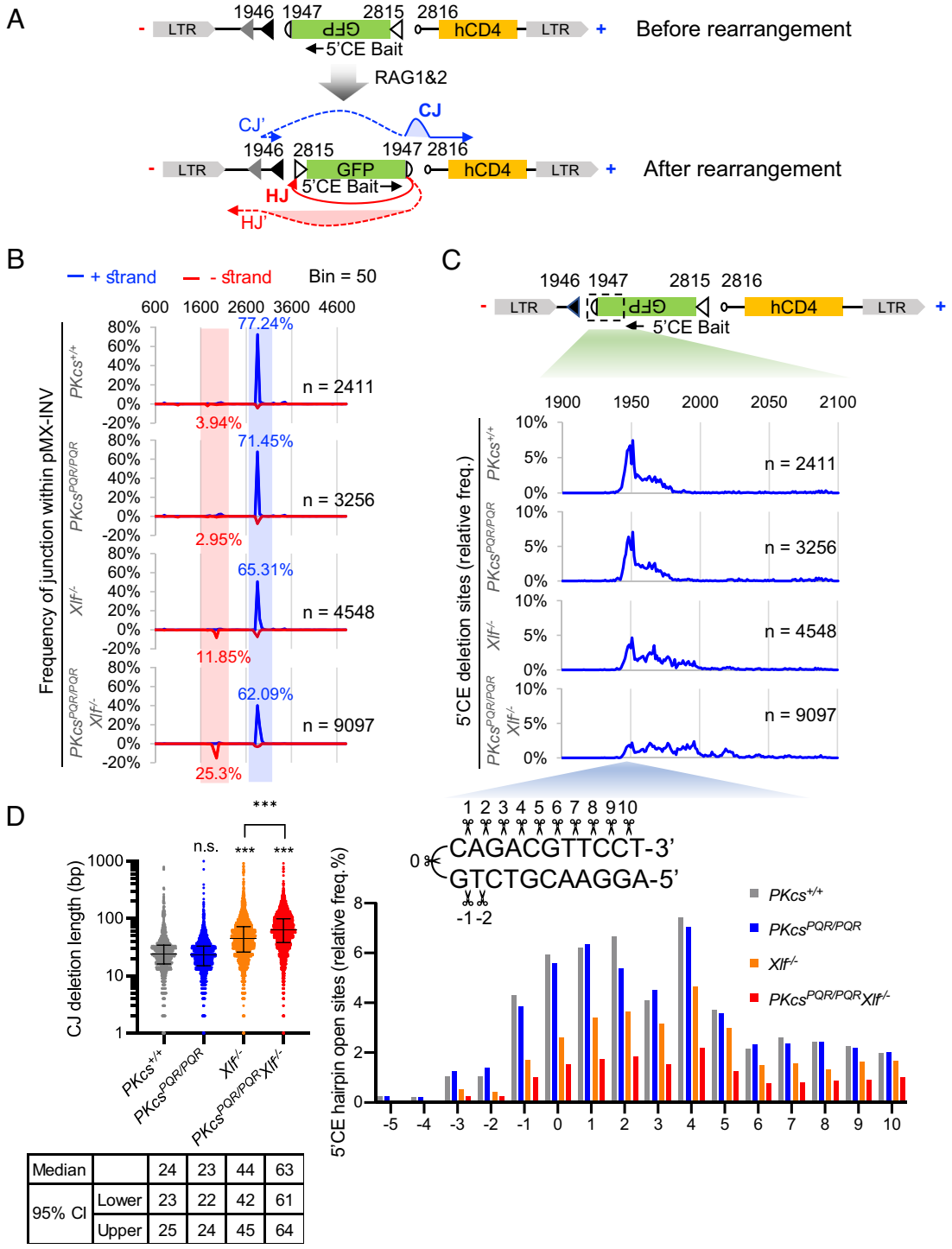

Median		24	23	44	63
95% CI	Lower	23	22	42	61
	Upper	25	24	45	64

Fig. 3. HTGTS analyses using a CE bait break on pMX-INV substrate reveal large deletion in *DNA-PKcs*$^{PQR/PQR}$*Xlf*$^{-/-}$ B cells. (*A*) The diagram of the possible junctions recovered using a 5′CEs bait. The *Upper* panel shows unrearranged pMX-INV substrate and the *Lower* panel shows the RAG-mediated inversion of the pMX-INV. The location of canonical 5′ 12 RSS (black filled triangle), alternative pseudo-5′ 12RSS (gray triangle) and 3′ 23 RSS (open triangle), 5′CE (circle near 1,947), and 3′CE (circle near 2,816) is marked. (*B*) The total frequency in the 50 bp sliding bins among all junctions within the pMX-INV substrate was plotted as a function of location. The blue traces indicate preys aligned to the (+) strand (from left to right in *A*) and red traces indicate preys aligned to the (−) strand (from right to left in *A*). The accumulative frequencies of preys falling into the 3′CE region (near 2,816, canonical CJ, in blue-shaded area, CJ in *A*) or into the 5′SE (near 1,946, hybrid joints, in red-shaded area, HJ′ in *A*) are marked. The total number of junctions in each plot is marked on the lower right. (*C*, *Top*) The box shows the bait region plotted below. (*C*, *Middle*) The relative frequency of 5'CEs bait ends among all junctions within the pMX-INV substrate. (*C*, *Bottom*) Diagrams of aligned bp locations and sequence at the 5′CE, zoom-in frequency of the adjacent 15 bps around the opened hairpin end. (*D*) The distribution of CJ deletion length (bp). Deletions from both sides of the break were added together. Junctions that fall into the highly structured IRES region between GFP and hCD4 have been removed for deletion analyses. The lines indicate median with interquartile range. Mann–Whitney test was used to calculate the *P* value. n.s., no significant difference. ***$P < 0.001$. The pool of all data from each genotype (see *SI Appendix*, Fig. S3*A* for sample information) was plotted in *B*–*D*.

hairpins. In WT and *DNA-PKcs*$^{PQR/PQR}$ lines, most of the bait CEs were opened at or near the apex- from 0 to +4 bp from the apex (Fig. 3*C*). *Xlf*$^{-/-}$ cells had a broader distribution of the CE opening, suggesting end-resection potentially followed by delayed ligation. The most extensive resection was found in *DNA-PKcs*$^{PQR/PQR}$*Xlf*$^{-/-}$ cells and also extended to >50 or even 100 bp from the apex

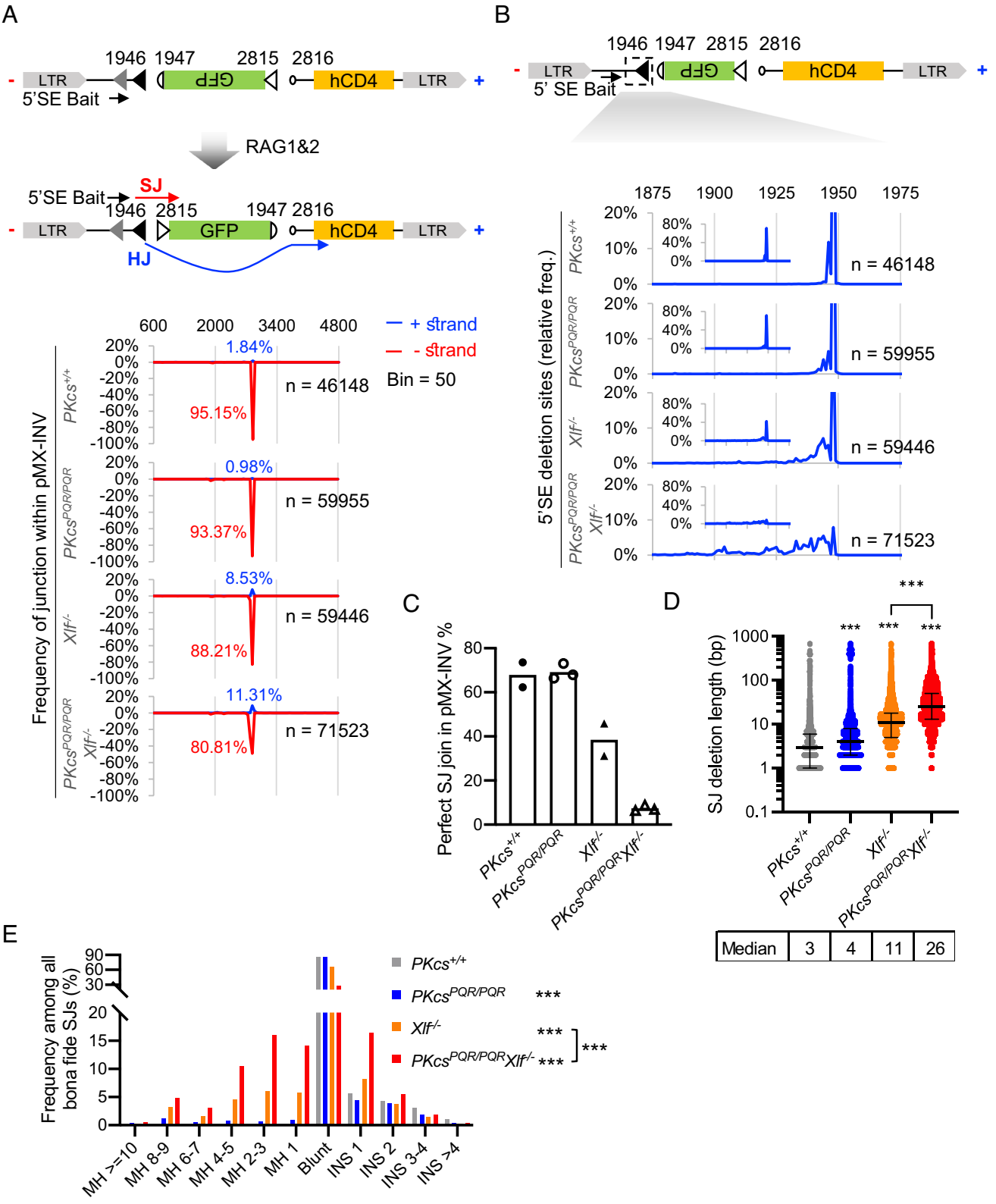

Fig. 4. HTGTS analyses using an SE bait break on pMX-INV substrate reveal large deletion in *DNA-PKcs*$^{PQR/PQR}$*Xlf*$^{-/-}$ B cells. (*A*, *Top*) The diagram of the possible junctions recovered using a 5′SEs bait. The location of canonical 5′ 12 RSS (black filled triangle), alternative pseudo 5′ 12RSS (gray triangle) and 3′ 23 RSS (open triangle), 5′CE (circle near 1,947), and 3′CE (circle near 2,816) is marked. (*A*, *Bottom*) The total frequency among all preys (50 bp bin) is plotted against the location on pMX-INV substrate. The red traces indicate preys aligned to the (−) strand (canonical SJ products) and the blue traces indicate preys aligned to the (+) strand (HJ products). The total number of junctions is shown on the right. (*B, Top*) Schematic diagram of pMX-INV substrate for V(D)J recombination with the location of the 5′ bait SE RSSs (the filled black triangles). (*B*, *Bottom*) The frequency of 5′SE terminal location among all junctions within pMX-INV substrate (1 bp bin). The baits were extensively resected in *DNA-PKcs*$^{PQR/PQR}$*Xlf*$^{-/-}$ B cells. (*C*) The frequency of precise SJ among all pMX-INV junctions recovered in each genotype. The bars represent the average of two or more samples per genotype. (*D*) The distribution of total SJ deletion length (bp). Deletions from both sides of the break were added together. The lines represent median and interquartile range. Mann–Whitney test was used to calculate the *P* value. (*E*) The distribution of all bona fide SJs within the pMX-INV substrate by junctional type (MH, microhomology. INS, insertion). Kolmogorov–Smirnov test was used to calculate the *P* value. ***$P < 0.001$. The pool of all data from each genotype (see *SI Appendix*, Fig. S3*A* for sample information) was plotted in *A, B, D,* and *E*.

(Fig. 3*C*). Correspondingly, the overall size of deletion at the CJs in *DNA-PKcs*$^{PQR/PQR}$*Xlf*$^{-/-}$ lines (median deletion = 63 bp, $P < 0.0001$ vs. *Xlf*$^{-/-}$) was significantly larger than those from *Xlf*$^{-/-}$ cells (median = 44 bp, $P < 0.0001$ vs. WT), which is larger than those from WT (median = 24 bp) and *DNA-PKcs*$^{PQR/PQR}$ cells (median = 23 bp, $P = 0.1800$ vs. WT) (Fig. 3*D* and *SI Appendix*, Table S2). This large deletion is consistent with the endogenous CJ junctions isolated from D–J rearrangements in B cells (Fig. 1*H* and *SI Appendix*, Table S1). At the B and T cell receptor loci, the CJ resides within the variable region exon. The large deletion could compromise the coding exon and explain the substantial developmental defects in *DNA-PKcs*$^{PQR/PQR}$*Xlf*$^{-/-}$ lymphocytes.

***DNA-PKcs*$^{PQR/PQR}$*Xlf*$^{-/-}$ Cells Have Increased Deletion at SJ of Chromosomal V(D)J Recombination.** CJ formation requires both end-processing (hairpin opening) and end-ligation. DNA-PKcs has been implicated in both end-processing and end-ligation. To understand whether PQR phosphorylation has an isolated impact on end-ligation independent of hairpin opening, we analyzed SJs using HTGTS and a 5′SE bait (Fig. 4*A*). With over 50,000 junction sequences from each genotype, wild-type and *DNA-PKcs*$^{PQR/PQR}$ lines had predominantly canonical SJs (>93%, red, negative strand) and very few HJs (<2%, blue, positive strand) (Fig. 4*A*). *Xlf*$^{-/-}$ cells had 88.2% SJs and 8.5% HJs, while *DNA-PKcs*$^{PQR/PQR}$*Xlf*$^{-/-}$ cells had only 80.8% SJs and 11.3% HJs (Fig. 4*A*). Analyses of bait 5'SEs from the junctions uncovered widespread large deletions in *DNA-PKcs*$^{PQR/PQR}$*Xlf*$^{-/-}$ cells beyond those found in *Xlf*$^{-/-}$ cells (Fig. 4*B*), suggesting end-ligation defects independent of hairpin opening. Correspondingly, while about 70% of all SJs recovered from wild-type and *DNA-PKcs*$^{PQR/PQR}$ lines in the HTGTS and 40% of SJs from *Xlf*$^{-/-}$ cells were precise, less than 10% of SJs recovered from *DNA-PKcs*$^{PQR/PQR}$*Xlf*$^{-/-}$ cells were precise (Fig. 4*C* and *SI Appendix*, Table S2). Analyses of endogenous SJs at the TCR Vβ14–Dβ1Jβ1 junction also uncovered a substantially reduced fidelity in *DNA-PKcs*$^{PQR/PQR}$*Xlf*$^{-/-}$ mice (22.6% fidelity) than *Xlf*$^{-/-}$ mice (48.3% fidelity) (*SI Appendix*, Table S1). The SJ base pair deletion in *DNA-PKcs*$^{PQR/PQR}$*Xlf*$^{-/-}$ cells (median = 26 bp, $P < 0.0001$) was also significantly larger than those from *Xlf*$^{-/-}$ cells (median = 11 bp) at the substrate and in vivo (Fig. 4*D* and *SI Appendix*, Tables S1 and S2). Consistent with previous findings (14, 53, 54), there is a reduction in SJ fidelity and joining when Xlf is not present. The residual SJs recovered from *Xlf*$^{-/-}$ and *DNA-PKcs*$^{PQR/PQR}$*Xlf*$^{-/-}$cells had an increased usage of MH with a more prominent shift toward MH usage in *DNA-PKcs*$^{PQR/PQR}$*Xlf*$^{-/-}$ cells (Fig. 4*E*). Our analyses further showed that DNA-PKcs PQR phosphorylation prevents excessive deletion during end-ligation in the Xlf-deficient background, providing an explanation for the severe developmental defects in *DNA-PKcs*$^{PQR/PQR}$*Xlf*$^{-/-}$ mice.

***DNA-PKcs*$^{PQR/PQR}$*Xlf*$^{-/-}$ Naïve B Cells Display CSR Defects Independent of Proliferation.** The chromosomal V(D)J joining defect in *DNA-PKcs*$^{PQR/PQR}$*Xlf*$^{-/-}$ pro-B lines can be attributed to impaired NHEJ, a repair pathway exclusively used during V(D)J recombination. To address whether loss of DNA-PKcs PQR phosphorylation has general NHEJ defects and is impaired for other forms of end-ligation, we analyzed IgH CSR. NHEJ is a prominent CSR repair pathway. CSR occurs at reduced levels in NHEJ-deficient cells via the Alt-EJ pathway that preferentially uses MH at the junction. By FACS, the ratio of antigen-experienced recirculated B cells (B220^{high}IgM^{+}) vs. naïve B cells (B220^{mid}IgM^{+}) was lower in *DNA-PKcs*$^{PQR/PQR}$*Xlf*$^{-/-}$ mice than that in *Xlf*$^{-/-}$ controls (*SI Appendix*, Fig. S4*A*), consistent with potential CSR defects. To analyze CSR, we isolated and activated wild-type, *DNA-PKcs*$^{PQR/PQR}$, *Xlf*$^{-/-}$, and *DNA-PKcs*$^{PQR/PQR}$*Xlf*$^{-/-}$ B cells with anti-CD40 and interleukin (IL)-4 to stimulate CSR to IgG1. As expected, *DNA-PKcs*$^{PQR/PQR}$ B cells underwent CSR efficiently, and *Xlf*$^{-/-}$ cells had a ~60% reduced CSR efficiency (Fig. 5 *A* and *B*). CSR in *DNA-PKcs*$^{PQR/PQR}$*Xlf*$^{-/-}$ cells was consistently yet moderately lower than that of *Xlf*$^{-/-}$ controls (Fig. 5 *A* and *B*). CSR requires cell proliferation, and the IgG1-positive cells accumulate with cell division. To control for the number of cell divisions, we stained the B cells with a cell surface dye (CTV) that is diluted upon each cell division and plotted CSR as a function of cell division. While CTV staining seems to suggest an increased proliferation in a subset of B cells from *DNA-PKcs*$^{PQR/PQR}$*Xlf*$^{-/-}$ mice, after gating the cells with the same number of cell divisions (within the red box) to control for proliferation, *DNA-PKcs*$^{PQR/PQR}$*Xlf*$^{-/-}$ cells still have much more prominent CSR defects than those of the *Xlf*$^{-/-}$ control (Fig. 5*C*). Thus, we conclude that in the Xlf-null background, loss of DNA-PKcs S2056 cluster phosphorylation causes proliferation-independent defects in CSR.

***DNA-PKcs*$^{PQR/PQR}$*Xlf*$^{-/-}$ B Cells Preferentially Lose CSR to Downstream Sε Switch Region.** Next, we analyzed >20,000 unique switch junctions from at least two, in most cases three, mice of each genotype (*SI Appendix*, Fig. S4*B*). We placed the bait break at the 5′ Sμ region and detected genome-wide translocations from baits (Fig. 6*A*). In all genotypes, the vast majority (>90%) of the preys were mapped within IgH (*SI Appendix*, Fig. S4*C*). Within IgH, the preys were mapped evenly into Sμ, Sγ1, and Sε in wild-type and *DNA-PKcs*$^{PQR/PQR}$ cells, reflecting internal deletion, and CSR to IgG1 and IgE, respectively (55). *Xlf*$^{-/-}$ and *DNA-PKcs*$^{PQR/PQR}$*Xlf*$^{-/-}$ cells showed a significant decrease in Sε preys and a relative increase in Sμ preys (*SI Appendix*, Fig. S4*D*). Given that the majority of the Sε switching events were achieved through sequential switching for Sμ to Sγ1, then to Sε, thus requiring two successful end-ligation events, preferential reduction of Sε preys has been seen in other NHEJ-deficient backgrounds also, including Xrcc4 null, DNA-PKcs-null, and DNA-PKcs T2609 phosphorylation site mutant mice (19, 56, 57). Three other indications of end-ligation defects are 1) increased end-resection measured by the accumulation of preys outside the core switch regions (19, 56, 57), 2) increased interchromosomal and intersister CSR with preys at the positive strand (55), and 3) increased use of MH at the junctions. For Sμ and Sγ1 preys, both *Xlf*$^{-/-}$ and *DNA-PKcs*$^{PQR/PQR}$*Xlf*$^{-/-}$ B cells displayed significantly increased resection over wild-type control or *DNA-PKcs*$^{PQR/PQR}$ cells (*SI Appendix*, Fig. S4 *E–H*). Only in the Sε preys were there significantly more resections (Fig. 6 *B* and *C*) and inverted junctions (Fig. 6*D*) in *DNA-PKcs*$^{PQR/PQR}$*Xlf*$^{-/-}$ B cells than those of the *Xlf*$^{-/-}$ controls. Moreover, there was a moderate shift toward MH usage in the Sμ–Sε CSR junctions, especially those at the negative strand (consistent with productive CSR), but the difference between *DNA-PKcs*$^{PQR/PQR}$*Xlf*$^{-/-}$ and *Xlf*$^{-/-}$ controls was not significant in Sμ internal deletion or Sμ–Sγ1 junctions (Fig. 6*E*, *SI Appendix*, Fig. S5 *A–C*, and Dataset S1). We conclude that DNA-PKcs PQR cluster phosphorylation is critical for chromosomal NHEJ during CSR in Xlf-deficient background by preferentially affecting CSR to distal Sε regions.

Discussion

Mammalian DNA-PKcs has two well-characterized phosphorylation clusters—the S2056 cluster and the T2609 cluster. Although not essential for NHEJ in human cell extracts in vitro (58), expression of human DNA-PKcs with alanine substitutions at the S2056 and/or T2609 cluster in DNA-PKcs-deficient CHO cells fails to

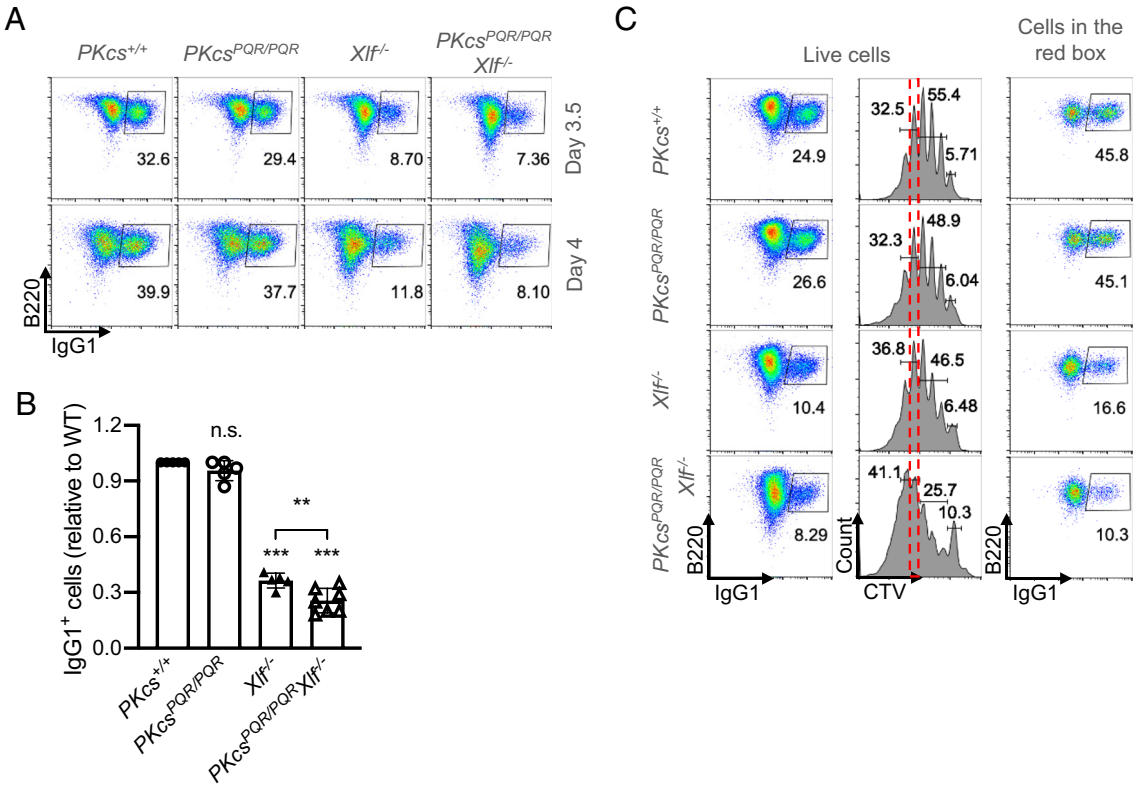

Fig. 5. S2056 cluster phosphorylation promotes CSR in *Xlf*$^{-/-}$ B cells. (*A*) Representative flow cytometric analyses of IgG1 CSR efficiency after 3.5 and 4 d of cytokine stimulation. The percentage of B220^{+}IgG1^{+} cells among all B cells was marked on each panel. (*B*) Quantification of B220^{+}IgG1^{+} B cell percentage on day 4 of stimulation. The bars represent the average and the SD of five or more mice per genotype. Student's *t* test was used to calculate the *P* value. n.s., no significant difference. $^{**}P < 0.01$, $^{***}P < 0.001$. (*C*) Representative flow cytometry analyses of IgG1 CSR efficiency after controlled for cell division (by CTV labeling). IgG1 CSR frequency of the cells that underwent five cell divisions (in the red box) was plotted on the right. One representative result from multiple independent repeats was shown.

restore IR resistance (31, 59–61) and Artemis-mediated end-processing (62, 63). Episomal end-joining analyses of DNA-PKcs with alanine substitutions at the T2609 or S2056 cluster show reduced end-ligation (59, 64, 65). Loss of S2056 or T2609 cluster phosphorylation alone has also been linked to moderate radiation sensitivity (33, 59, 64, 65). To determine whether autophosphorylation of DNA-PKcs has a role in physiological NHEJ required during lymphocyte development independent of its kinase activity, we generated a mouse model with knock-in alanine substitutions at the S2056 cluster or T2609 cluster (32–34, 49). Our results suggest that alanine substitutions at the S2056 cluster (*DNA-PKcs*$^{PQR/PQR}$) have no measurable impact on both V(D)J recombination and CSR recombination efficiency or junction fidelity (33), leaving the physiological importance of S2056 cluster phosphorylation unknown. Here, we report that in Xlf-deficient mice, loss of DNA-PKcs S2056 cluster phosphorylation compromises B and T lymphocyte development at the stage of V(D)J recombination. Moreover, the severe development defects in *DNA-PKcs*$^{PQR/PQR}$*Xlf*$^{-/-}$ lymphocytes cannot be explained by lack of ligation alone. Instead, we noted large deletions in CJs and SJs recovered from *DNA-PKcs*$^{PQR/PQR}$*Xlf*$^{-/-}$ cells, suggesting excessive deletion as a cause for the failed development. This is in sharp contrast with previously characterized NHEJ-deficient models including the ATM/XLF double-deficient mice (22), where unrepaired CEs and SEs are readily detectable, suggesting that ATM and DNA-PKcs-PQR phosphorylation act through different mechanisms to promote NHEJ in Xlf-deficient cells. This role of S2056 cluster phosphorylation to suppress excessive end-resection is not limited to V(D)J recombination. *DNA-PKcs*$^{PQR/PQR}$*Xlf*$^{-/-}$ B cells also display defects in IgH CSR that preferentially affect distal switching to Sε indicated by increased resection and inverted junctions. Thus, our results provide the evidence for a measurable role of S2056 cluster phosphorylation in chromosomal end-ligation. The genetic systems and high-throughput junctional analyses developed here could also be used to characterize subtle DSB repair defects, especially those compromising junction fidelity without joining efficiency in the future.

What is the role of the PQR phosphorylation? DNA-PKcs has been implicated in both end-processing and end-ligation. For end-processing, previous functional analyses of DNA-PKcs-null and kinase-dead models (4, 29, 66, 67) and recent structural studies (68, 69) provide a consistent model in which DNA-PKcs protein serves as a platform to physically recruit and activate Artemis endonuclease for end-processing. This role of DNA-PKcs requires DNA-PKcs protein and ATP hydrolysis by either ATM or DNA-PK. As such, the coding hairpin is opened in *DNA-PKcs*$^{KD/KD}$ cells lacking DNA-PKcs activity as long as ATM kinase activity is available (29). In cells with WT DNA-PKcs and its kinase activity, ATM kinase activity becomes dispensable for hairpin opening (35, 49, 50). DNA-PKcs kinase inhibitors also fail to block hairpin openings in otherwise WT cells (49). Which phosphorylation sites are important? Consistent with prior studies on episomal substrates (33), we did not detect any measurable impact of the S2056 cluster phosphorylation on hairpin opening in vivo. In this regard, the T2609 cluster (62) can be phosphorylated by either DNA-PKcs or ATM kinase and has been linked to Artemis activation (70, 71). How DNA-PKcs promotes end-ligation is more complicated. Genetically, DNA-PKcs null mice have at most a moderate end-ligation defect characterized by a mild decrease of fidelity (66, 67). In contrast, the expression of kinase-dead DNA-PKcs

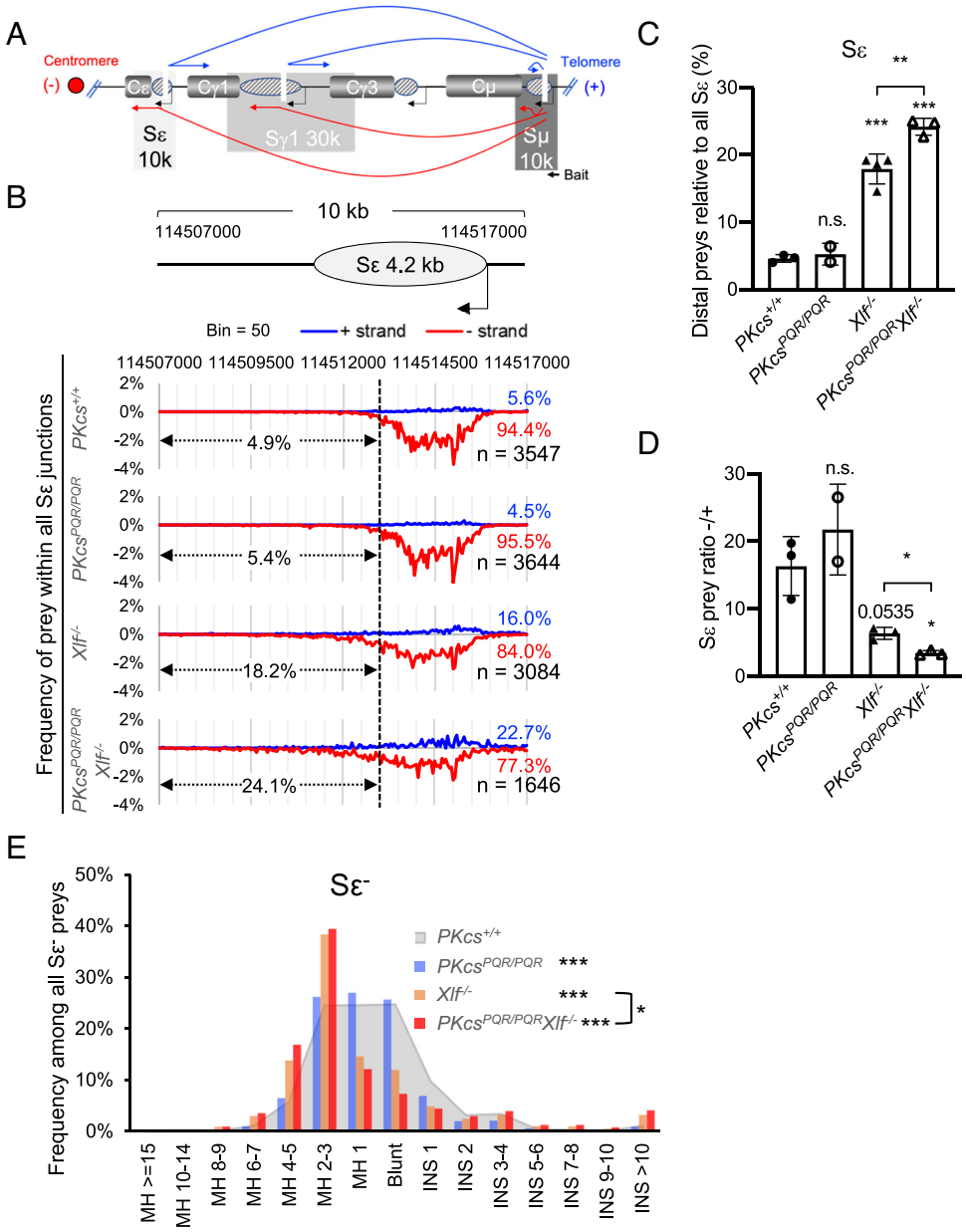

Fig. 6. S2056 cluster phosphorylation preferentially affects CSR to Sε in *Xlf*$^{-/-}$ B cells. (*A*) Diagram of the murine IgH locus with the location of Sμ (dark gray), Sγ1 (gray), and Sε (light gray). The bait site at the 5′Sμ region is also marked. Since IgH resides on the negative strand of murine chromosome 12, the preys on the (−) strand (red arrows, bona fide CSR junctions) reflect normal internal deletion and CSR, and the preys on the (+) strand (blue arrows) indicate inversion or interchromosomal junction with sister or homologous chromosome. (*B*) The total frequency of preys within Sε region (bin size = 50 bp). The data from multiple mice of the same genotype were pooled and plotted together (see *SI Appendix*, Fig. S4*B* for sample information). Schematic of the Sε region is at the top. All (−, red, below zero) and (+, blue, above zero) strand preys add up to 100%. For each genotype, the percentage of (+) strand (blue) and (−) strand (red) junctions and total number are marked at the right. The values between y-axis and the dashed line (114,507,000~114,513,000) indicate the percentage of preys that fall outside the core Sε region. (*C*) Relative frequency of distal preys among the preys in Sε region. (*D*) The (−) vs. (+) strand prey ratio in Sε region. The bars in *C* and *D* represent the average and SD of several independently derived libraries by genotype, respectively. Student's *t* test was used to calculate the *P* value. n.s., no significant difference. **P* < 0.05, ***P* < 0.01, ****P* < 0.001. (*E*) The distribution of all Sε junctions at the minus strand by junctional type (MH, microhomology. INS, insertion). This graph represents the pool of at least two independent libraries (*SI Appendix*, Fig. S4*B*) of each genotype. Kolmogorov–Smirnov test was used to calculate the *P* value. **P* < 0.05, ****P* < 0.001.

completely blocks end-ligation (29). Cryo-EM analyses show that the apo form of DNA-PK holoenzyme blocks the DNA ends, and DNA-PKcs activation and the concurrent autophosphorylation trigger allosteric changes that expose the DNA ends (68, 69). Among the two major phosphorylation clusters, the S2056 cluster is mainly phosphorylated by DNA-PK, while the T2609 cluster has been reported to be phosphorylated by ATM, DNA-PKcs, or ATR (10). Nevertheless, alanine substitutions at either the T2609 or S2056 cluster have a very moderate effect on chromosomal V(D)J recombination (33, 49, 57). ATM inhibitor also has no effect on end-ligation in S2056 cluster phosphorylation–deficient mice (33). But, ATM and DNA-PKcs inhibitors block end-ligation in cells lacking ABCDE cluster phosphorylation (49), suggesting that additional sites might be involved or the inhibitors might trigger a structure status that requires T2609 cluster phosphorylation for ligation. During CSR when hairpinned ends are not a concern, T2609 cluster phosphorylation reduces MH usage, but S2056 cluster alanine substitution has no measurable impact (33). Together, the results suggest a more prominent role of T2609 cluster phosphorylation in end-ligation than that of the S2056

cluster. It also suggests that a role of DNA-PKcs phosphorylation at the S2056 cluster in end-ligation or end-release might be masked by other phosphorylation events (T2609 or others) or by other factors (e.g., XLF).

So how does PQR phosphorylation of DNA-PKcs prevent excessive deletion? To understand the role of DNA-PKcs in end-ligation, DNA-PKcs has been deleted in several sensitizing backgrounds. Among them, loss of XLF and deletion/inhibition of ATM kinase independently abolished end-ligation in DNA-PKcs-null cells (24, 25, 35, 48). Moreover, ATM kinase inhibition or deletion also severely compromised end-ligation in T2609A mutant murine cells (34, 49, 57). Yet, ATM inhibition has no measurable impact on CSR or chromosomal V(D)J recombination of S2056 cluster mutant murine cells (33), suggesting that DNA-PKcs T2609 and S2056 cluster phosphorylation have distinct roles in NHEJ. Single-molecule (72) and structural analyses (28) provide evidence for a long-range synaptic NHEJ complex that brings together the KU at the two ends by four interactions 1) PAXX bridges the KU of each end (41, 44, 45, 73, 74); 2) the XLF dimer interacts with the KU on each end with the C-terminal tails (74); 3) Lig4/XRCC4–XLF–XRCC4/Lig4 with Lig4 binding to KU on each end, and 4) in parallel the two DNA-PKcs molecules bring the two ends together through direct interaction or reach out by the Ku80 C-terminal domains (28, 75). Among them, both 2 and 3 require XLF, and 3 also requires a structural function of DNA Ligase 4. In this context, Lig4 protein (but not its enzymatic activity) is important for PQR phosphorylation (76, 77), consistent with a model in which the stabilization of the XLF–XRCC4–Lig4 bridge allows additional time for DNA-PKcs intermolecular autophosphorylation. Given that the S2056 cluster resides in a flexible loop with major movement upon DNA-PKcs activation and concurrent autophosphorylation, one possibility might be that the S2056 cluster phosphorylation might preferentially change the conformation of DNA-PKcs to a "pro-ligation" mode. This conformation might promote end-ligation or serve a redundant function with XLF in the long-range NHEJ complex. In the absence of both XLF and PQR phosphorylation, the transition to the ligation complex is delayed and MRN might be activated to cleave off the KU. As such, most joins recovered contained additional 30 to 40 bp deletions—consistent with the footprint of KU+DNA-PKcs (68, 69). Together, the data suggest a distinct role of S2056 vs. T2609 cluster phosphorylation of DNA-PKcs and provide the physiological role of S2056 cluster phosphorylation in vivo.

Materials and Methods

Mice. *DNA-PKcs*$^{+/PQR}$ (33), *Xlf*$^{+/-}$ (78), *Xrcc4*$^{+/-}$ (7), and *Eμ-Bcl2*$^{+}$ (79) mice have been described previously. All animal work has been conducted in a pathogen-free facility, and all the procedures were approved by the Institutional Animal Care and Use Committee at Columbia University Medical Center.

Lymphocyte Development and Hematopoiesis Analyses. Single-cell suspensions were prepared from the bone marrow, spleen, and thymus of young adult (< 14 wk) mice. Splenocytes were treated with red blood cell lysis buffer (Lonza ACK Lysis Buffer) for 4 to 5 min at room temperature to remove enucleated erythrocytes. Approximately 2.5 × 10^6 cells were stained using fluorescence-conjugated antibodies and analyzed by flow cytometry. For lymphocyte development, the following antibody mixtures were used for B cell (FITC rat anti-mouse CD43, BD Pharmingen 553270; PE goat anti-mouse IgM, Southern Biotech 1020-09; PE-Cy5 anti-Hu/Mo CD45R (B220), eBioscience 15-0452-83; and APC anti-mouse TER-119, BioLegend 116212) and T cell (FITC anti-mouse CD8α, BioLegend 100706; PE rat anti-mouse CD4, BD Pharmingen 557308; PE/Cy5 anti-mouse TER-119, eBioscience 15-5921-82; and APC hamster anti-mouse TCRβ, BD Pharmingen 553174) analyses. For hematopoietic stem and progenitor cell (HSPC) analysis, bone marrow cells were first stained with a cocktail of biotin-labeled primary antibodies containing mouse-specific lineage markers: anti-B220 (BioLegend, 103204), anti-CD4 (BioLegend, 100404), anti-CD8α (BioLegend, 100704), anti-CD3ε (BioLegend, 100304), anti-CD5 (BD Pharmingen, 553018), anti-Ly-6G/Ly-6C (Gr-1) (BioLegend, 108404), and anti-TER-119 (BioLegend, 116204) at 4 °C for 0.5 h, before being washed and stained with a cocktail of directly conjugated antibodies including FITC anti-mouse CD34 (eBioscience, 11-0341-82), PE anti-mouse Ly-6A/E (Sca-1) (BioLegend, 108108), PE/Cy5 anti-mouse CD150 (BioLegend, 115912), PE/Cy7 anti-mouse CD16/32 (BioLegend, 101318), APC anti-mouse CD117 (c-Kit) (BioLegend, 135108), APC/Cy7 Streptavidin (BioLegend, 405208), Pacific Blue anti-mouse CD48 (BioLegend, 103418), and Brilliant Violet 510 anti-mouse CD41 (BioLegend, 133923) at 4 °C for 0.5 h. For erythroid development analysis, bone marrow cells were stained with an erythroid cocktail (PE-Cy5 anti-Hu/Mo CD45R (B220) (as above); PE/Cy7 anti-mouse TER-119, BioLegend 116222; APC anti-mouse Ly-6G/Ly-6C (Gr-1), eBioscience 17-5931-81; Alexa Fluor 700 anti-mouse CD11b, eBioscience 56-0112-82; Pacific Blue anti-mouse CD90.2 (Thy1.2), BioLegend 140306; and Brilliant Violet 510 anti-mouse CD71, BioLegend 113823). The dead cells and debris were excluded based on their high side scatter and low forward scatter. Anti-Ter119 (an early proerythroblast to mature erythrocyte marker) antibody was used to exclude erythrocytes from bone marrow and thymocytes analyses in Fig. 1*B*. Anti-CD71 and anti-Ter119 were used to identify differentiation-stage-specific subsets of erythrocytes as shown in *SI Appendix*, Fig. 1*G* (80). Flow cytometry was performed on FACSCalibur (BD Biosciences) or Attune flow cytometer (Thermo Fisher), and data were processed by FlowJo.

Endogenous V(D)J Recombination Analysis. To access the V(D)J recombination in vivo, the V(D)J recombination junctions in IgH locus and TCRβ locus were isolated from bone marrow cells and thymic cells, respectively. To isolate the nonselective D_H–J_H junctions in B cells, nesting PCR was performed with a first set of primers JH_DQ52 (5′-TGATAGGCACCCAAGTACACTA-3′) and JH4 Int (5′-CCTCTCCAGTTTCGGCTGAATCC-3′) and a second set with JH_DQ52 primer and JH4E (5′-AGGCTCTGAGATCCCTAGACAG-3′). The generated amplicons correspond to rearrangements with four bands of sizes less than 4 kb. Only the DQ52 to JH4 rearrangement (567 bp) was gel purified, cloned into pGEM-T Easy vector (Promega), and sequenced. In T cells, the Vβ14 to Dβ1Jβ1 SJs were amplified using primers Vβ14-DJ1_SJ_F (5′-GGCAAGGGCAAAGCTAGGCTAGAT-3′) and Vβ14-DJ1_SJ_R (5′-GCATGCCCAGCGTACCTCAATAG-3′). The amplified product (~722 bp) was gel purified, cloned into pGEM-T Easy vector, and sequenced. To examine junctional diversity, the deletion and the palindromic element and nontemplate nucleotide addition were identified by alignment of unique junctions.

Chromosomal V(D)J Recombination Assay. Total bone marrow was isolated from 4-wk-old mice carrying the Eμ-Bcl2 transgene and infected with retrovirus-encoding v-abl kinase and transformed clones were isolated as detailed before (50). Transformed v-abl B cells were cultured in DMEM with 15% fetal bovine serum for at least two months to achieve clonality and stable transformation. Chromosomal V(D)J recombination substrate (pMX-INV) (50) was integrated into each cell line via retrovirus infection and positively identified via magnetic bead purification. Southern blot was used to verify a single copy of the integrated substrate when needed. V(D)J recombination with integrated substrate was carried out as before (22, 50). Briefly, v-abl-transformed B cells with stable integration of the substrate were treated with STI571 (3 μM, Novartis Pharmaceuticals) for 2 and 4 d. FACS analyses were carried out for GFP induction and genomic DNA was collected for southern blot. For southern blot, 25 μg DNA was digested with either EcoRV or EcoRV + NcoI and probed with C4 probe (22, 50). The C4 probe is the 982 bp fragment generated by digestion with HindIII and NheI of the pMX-INV substrate plasmid (22, 50).

Class-Switch Recombination and Cell Trace Violet Assay. The splenic CD43 cells, isolated from 6 to 14-wk-old mice with CD43 magnetic beads (MACS, Miltenyi Biotec), were cultured in RPMI medium (Gibco) supplemented with 15% fetal bovine serum, 1 μg/mL anti-CD40 (BD Pharmingen, 553721), and 20 ng/mL IL-4 (R&D, 404-ML-050) at a density of 1 × 10^6 cells/mL. The cells were analyzed by flow cytometry after staining for IgG1 (FITC anti-IgG1, BD Pharmingen 553443) and B220 (PE/Cy7 anti-B220, BioLegend 103222) on days 3 and 4. For the cell trace violet (CTV) staining, purified CD43$^-$ B cells were incubated at 6 × 10^6 cells/mL in 1 mL PBS with 5 μM CTV dye (Thermo Fisher) for 20 min at 37 °C,

following the standard protocol with two additional washes with prewarmed medium. The CTV-stained B cells were stimulated with anti-CD40 antibody and IL-4 as detailed above and subjected to flow cytometry after staining for IgG1 and B220 on day 3.5.

HTGTS. HTGTS was performed as described (18, 55, 81, 82). To study the junctions from chromosomal V(D)J recombination, 20 μg genomic DNA from v-abl-transformed B cells with stable integration of the pMX- INV substrate was sonicated. For the coding joint junctions, the biotin-labeled primer (/5Bios/ACAACCACTACCTGAGCACC) was used for the linear amplification and another primer (5′-CAAAGACCCCAACGAGAAGC-3′) was applied for nested amplification. Germline (unrearranged) sequence was removed with BstBI (New England Biolabs) digestion. For signal joint junctions, sonicated DNA was linearly amplified with primer (/5Bios/GGCAGCCTACCAAGAACAAC) and nested amplified with primer (5′-CGGTGGTACCTCACCCTTA-3′). Germline sequence was removed with EcoRI (New England Biolabs) digestion. For the sequence analysis, the pMX-INV substrate sequence was added as an additional chromosome on top of the mm10 genome during the alignment process. To study the junctions from CSR, 20 μg genomic DNA from CD43$^-$ B cells stimulated with anti-CD40 and IL-4 for 4 d was sonicated and amplified with Sμ-specific biotin primer (/5Bios/CAGACCTGGGAATGTATGGT) and nested (5′-CACACAAAGACTCTGGACCTC-3′) primers. AflII (New England Biolabs) was used to remove germline sequence. Since all our experimental mice are of pure 129 background, the IgH switch region (from JH4 to the last Cα exon, chr12: 114494415–114666816) of the C57/BL6-based mm9 was replaced with the corresponding region in the AJ851868.3 (GenBank accession no. AJ851868.3) 129 IgH sequence (1415966–1592715) to generate the mm9sr (switch region replacement) genome.

Sequences were analyzed as detailed before (18, 55) with the pipeline deposited on GitHub (https://github.com/robinmeyers/transloc_pipeline). Best-path searching algorithm [related to YAHA (83)] was used to select optimal junctions from Bowtie2-reported top alignments (alignment score > 50). The reads were then filtered to exclude misprimed events, germline sequence, competing prey, and duplicated reads. A "duplicate read" was defined by the coordination of a bait and prey alignment within 2 nt of another bait and prey alignment. Since signal joint read number was very low after applying deduplication filter, this filter was not used for SJ analysis. For SJ and CJ deletion analyses, the deletion size was capped at 1,000 bp. Since some switch region sequences are very repetitive, the alignments in those regions were filtered out by the mappability filter. But they do unequivocally map to an individual switch region, so to plot all the switch region junctions, we added the ones filtered out by the mappability filter back after deduplication (55). MHs are defined as regions of 100% homology between the bait and prey-break site. Insertions are defined as regions containing nucleotides that map to neither the bait nor prey-break site. Blunt junctions are considered to have no MHs or insertions. The HTGTS data reported in this paper have been deposited in the Gene Expression Omnibus (https://www.ncbi.nlm.nih.gov/geo/) under accession number GSE228850 (82).

Data, Materials, and Software Availability. Sequencing Data have been deposited in NCBI Gene Expression Omnibus GEO (GSE228850) (82). All study data are included in the article and/or supporting information.

ACKNOWLEDGMENTS. We thank the members of the Zha Lab for helpful discussions and advice on lymphocyte development and sequence analyses. Due to space limitations, we could not cite all the original publications and cite reviews when necessary. This work was supported by NIH R01CA275184 and 5R01CA158073, and P01CA174653 to (S.Z.). Y.Z. is a fellow of Cancer Research Institute. This research was funded in part through the NIH/NCI Cancer Center Support Grant P30CA013696 to the Herbert Irving Comprehensive Cancer Center of Columbia University.

Author affiliations: [a]Institute for Cancer Genetics, Vagelos College of Physicians and Surgeons, Columbia University, New York City, NY 10032; [b]Department of Biology, Barnard College, Columbia University, New York City, NY 10027; [c]Division of Pediatric Oncology, Hematology and Stem Cell Transplantation, Department of Pediatrics, Vagelos College of Physicians & Surgeons, Columbia University, New York City, NY 10032; [d]Department of Pathology and Cell Biology, Vagelos College of Physicians and Surgeons, Columbia University, New York City, NY 10032; and [e]Department of Immunology and Microbiology, Vagelos College of Physicians and Surgeons, Columbia University, New York City, NY 10032

1. M. Mohrin *et al.*, Hematopoietic stem cell quiescence promotes error-prone DNA repair and mutagenesis. *Cell Stem. Cell* **7**, 174–185 (2010).
2. D. J. Rossi *et al.*, Deficiencies in DNA damage repair limit the function of haematopoietic stem cells with age. *Nature* **447**, 725–729 (2007).
3. C. H. Bassing, F. W. Alt, The cellular response to general and programmed DNA double strand breaks. *DNA Repair (Amst)* **3**, 781–796 (2004).
4. Y. Ma, U. Pannicke, K. Schwarz, M. R. Lieber, Hairpin opening and overhang processing by an Artemis/DNA-dependent protein kinase complex in nonhomologous end joining and V(D)J recombination. *Cell* **108**, 781–794 (2002).
5. S. Rooney *et al.*, Leaky Scid phenotype associated with defective V(D)J coding end processing in Artemis-deficient mice. *Mol. Cell* **10**, 1379–1390 (2002).
6. D. E. Barnes, G. Stamp, I. Rosewell, A. Denzel, T. Lindahl, Targeted disruption of the gene encoding DNA ligase IV leads to lethality in embryonic mice. *Curr. Biol.* **8**, 1395–1398 (1998).
7. Y. Gao *et al.*, A critical role for DNA end-joining proteins in both lymphogenesis and neurogenesis. *Cell* **95**, 891–902 (1998).
8. D. Buck *et al.*, Severe combined immunodeficiency and microcephaly in siblings with hypomorphic mutations in DNA ligase IV. *Eur. J. Immunol.* **36**, 224–235 (2006).
9. K. M. Frank *et al.*, Late embryonic lethality and impaired V(D)J recombination in mice lacking DNA ligase IV. *Nature* **396**, 173–177 (1998).
10. X. S. Wang, B. J. Lee, S. Zha, The recent advances in non-homologous end-joining through the lens of lymphocyte development. *DNA Repair (Amst)* **94**, 102874 (2020).
11. C. T. Yan *et al.*, IgH class switching and translocations use a robust non-classical end-joining pathway. *Nature* **449**, 478–482 (2007).
12. Q. Pan-Hammarstrom *et al.*, Impact of DNA ligase IV on nonhomologous end joining pathways during class switch recombination in human cells. *J. Exp. Med.* **201**, 189–194 (2005).
13. F. Rucci *et al.*, Homozygous DNA ligase IV R278H mutation in mice leads to leaky SCID and represents a model for human LIG4 syndrome. *Proc. Natl. Acad. Sci. U.S.A.* **107**, 3024–3029 (2010).
14. G. Li *et al.*, Lymphocyte-specific compensation for XLF/cernunnos end-joining functions in V(D)J recombination. *Mol. Cell.* **31**, 631–640 (2008).
15. S. Zha, F. W. Alt, H. L. Cheng, J. W. Brush, G. Li, Defective DNA repair and increased genomic instability in cernunnos-XLF-deficient murine ES cells. *Proc. Natl. Acad. Sci. U.S.A.* **104**, 4518–4523 (2007).
16. S. Rooney, F. W. Alt, J. Sekiguchi, J. P. Manis, Artemis-independent functions of DNA-dependent protein kinase in Ig heavy chain class switch recombination and development. *Proc. Natl. Acad. Sci. U.S.A.* **102**, 2471–2475 (2005).
17. S. Franco *et al.*, DNA-PKcs and Artemis function in the end-joining phase of immunoglobulin heavy chain class switch recombination. *J. Exp. Med.* **205**, 557–564 (2008).
18. J. Hu *et al.*, Detecting DNA double-stranded breaks in mammalian genomes by linear amplification-mediated high-throughput genome-wide translocation sequencing. *Nat. Protoc.* **11**, 853–871 (2016).
19. J. L. Crowe *et al.*, Kinase-dependent structural role of DNA-PKcs during immunoglobulin class switch recombination. *Proc. Natl. Acad. Sci. U.S.A.* **115**, 8615–8620 (2018), 10.1073/pnas.1808490115.
20. S. Franco, F. W. Alt, J. P. Manis, Pathways that suppress programmed DNA breaks from progressing to chromosomal breaks and translocations. *DNA Repair (Amst)* **5**, 1030–1041 (2006).
21. S. Franco *et al.*, H2AX prevents DNA breaks from progressing to chromosome breaks and translocations. *Mol. Cell* **21**, 201–214 (2006).
22. S. Zha *et al.*, ATM damage response and XLF repair factor are functionally redundant in joining DNA breaks. *Nature* **469**, 250–254 (2011).
23. E. J. Gapud, B. P. Sleckman, Unique and redundant functions of ATM and DNA-PKcs during V(D)J recombination. *Cell Cycle* **10**, 1928–1935 (2011).
24. S. Zha *et al.*, Ataxia telangiectasia-mutated protein and DNA-dependent protein kinase have complementary V(D)J recombination functions. *Proc. Natl. Acad. Sci. U.S.A.* **108**, 2028–2033 (2011).
25. E. Callen *et al.*, Essential role for DNA-PKcs in DNA double-strand break repair and apoptosis in ATM-deficient lymphocytes. *Mol. Cell* **34**, 285–297 (2009).
26. D. A. Reid *et al.*, Organization and dynamics of the nonhomologous end-joining machinery during DNA double-strand break repair. *Proc. Natl. Acad. Sci. U.S.A.* **112**, E2575–2584 (2015).
27. T. G. Graham, J. C. Walter, J. J. Loparo, Two-stage synapsis of DNA ends during non-homologous end joining. *Mol. Cell* **61**, 850–858 (2016).
28. S. Chen *et al.*, Structural basis of long-range to short-range synaptic transition in NHEJ. *Nature* **593**, 294–298 (2021).
29. W. Jiang *et al.*, Differential phosphorylation of DNA-PKcs regulates the interplay between end-processing and end-ligation during nonhomologous end-joining. *Mol. Cell* **58**, 172–185 (2015).
30. X. Chen *et al.*, Structure of an activated DNA-PK and its implications for NHEJ. *Mol. Cell* **81**, 801–810.e3 (2021), 10.1016/j.molcel.2020.12.015.
31. K. Meek, S. Gupta, D. A. Ramsden, S. P. Lees-Miller, The DNA-dependent protein kinase: The director at the end. *Immunol. Rev.* **200**, 132–141 (2004).
32. Z. Shao *et al.*, DNA-PKcs has KU-dependent function in rRNA processing and haematopoiesis. *Nature* **579**, 291–296 (2020).
33. W. Jiang *et al.*, Phosphorylation at S2053 in murine (S2056 in human) DNA-PKcs is dispensable for lymphocyte development and class switch recombination. *J. Immunol.* **203**, 178–187 (2019).
34. S. Zhang *et al.*, Congenital bone marrow failure in DNA-PKcs mutant mice associated with deficiencies in DNA repair. *J. Cell Biol.* **193**, 295–305 (2011).
35. E. J. Gapud *et al.*, Ataxia telangiectasia mutated (Atm) and DNA-PKcs kinases have overlapping activities during chromosomal signal joint formation. *Proc. Natl. Acad. Sci. U.S.A.* **108**, 2022–2027 (2011).
36. C. Lescale *et al.*, RAG2 and XLF/cernunnos interplay reveals a novel role for the RAG complex in DNA repair. *Nat. Commun.* **7**, 10529 (2016).
37. C. Beck, S. Castaneda-Zegarra, C. Huse, M. Xing, V. Oksenych, Mediator of DNA damage checkpoint protein 1 facilitates V(D)J recombination in cells lacking DNA repair factor XLF. *Biomolecules* **10**, 60 (2019).

38. V. Oksenych *et al.*, Functional redundancy between repair factor XLF and damage response mediator 53BP1 in V(D)J recombination and DNA repair. *Proc. Natl. Acad. Sci. U.S.A.* **109**, 2455–2460 (2012).
39. X. Liu *et al.*, Overlapping functions between XLF repair protein and 53BP1 DNA damage response factor in end joining and lymphocyte development. *Proc. Natl. Acad. Sci. U.S.A.* **109**, 3903–3908 (2012).
40. P. J. Hung *et al.*, MRI Is a DNA damage response adaptor during classical non-homologous end joining. *Mol. Cell* **71**, 332–342.e338 (2018).
41. V. Kumar, F. W. Alt, R. L. Frock, PAXX and XLF DNA repair factors are functionally redundant in joining DNA breaks in a G1-arrested progenitor B-cell line. *Proc. Natl. Acad. Sci. U.S.A.* **113**, 10619–10624 (2016).
42. C. Lescale *et al.*, Specific roles of XRCC4 paralogs PAXX and XLF during V(D)J recombination. *Cell Rep.* **16**, 2967–2979 (2016), 10.1016/j.celrep.2016.08.069.
43. S. K. Tadi *et al.*, PAXX is an accessory c-NHEJ factor that associates with Ku70 and has overlapping functions with XLF. *Cell Rep.* **17**, 541–555 (2016).
44. P. J. Hung *et al.*, Deficiency of XLF and PAXX prevents DNA double-strand break repair by non-homologous end joining in lymphocytes. *Cell Cycle* **16**, 286–295 (2017).
45. X. Liu, Z. Shao, W. Jiang, B. J. Lee, S. Zha, PAXX promotes KU accumulation at DNA breaks and is essential for end-joining in XLF-deficient mice. *Nat. Commun.* **8**, 13816 (2017).
46. M. Xing, V. Oksenych, Genetic interaction between DNA repair factors PAXX, XLF, XRCC4 and DNA-PKcs in human cells. *FEBS Open Bio.* **9**, 1315–1326 (2019).
47. B. Ruis, A. Molan, T. Takasugi, E. A. Hendrickson, Absence of XRCC4 and its paralogs in human cells reveal differences in outcomes for DNA repair and V(D)J recombination. *DNA Repair (Amst)* **85**, 102738 (2020).
48. V. Oksenych *et al.*, Functional redundancy between the XLF and DNA-PKcs DNA repair factors in V(D) J recombination and nonhomologous DNA end joining. *Proc. Natl. Acad. Sci. U.S.A.* **110**, 2234–2239 (2013).
49. B. S. Lee *et al.*, Functional intersection of ATM and DNA-PKcs in coding end joining during V(D)J recombination. *Mol. Cell Biol.* **33**, 3568–3579 (2013).
50. A. L. Bredemeyer *et al.*, ATM stabilizes DNA double-strand-break complexes during V(D)J recombination. *Nature* **442**, 466–470 (2006).
51. M. A. Oettinger, Activation of V(D)J recombination by RAG1 and RAG2. *Trends Genet.* **8**, 413–416 (1992).
52. Z. Liang *et al.*, Ku70 suppresses alternative end joining in G1-arrested progenitor B cells. *Proc. Natl. Acad. Sci. U.S.A.* **118**, e2103630118 (2021).
53. B. Zhao *et al.*, The essential elements for the noncovalent association of two DNA ends during NHEJ synapsis. *Nat. Commun.* **10**, 3588 (2019).
54. B. Zhao, E. Rothenberg, D. A. Ramsden, M. R. Lieber, The molecular basis and disease relevance of non-homologous DNA end joining. *Nature reviews. Mol. Cell Biol.* **21**, 765–781 (2020).
55. J. Dong *et al.*, Orientation-specific joining of AID-initiated DNA breaks promotes antibody class switching. *Nature* **525**, 134–139 (2015).
56. X. S. Wang *et al.*, CtIP-mediated DNA resection is dispensable for IgH class switch recombination by alternative end-joining. *Proc. Natl. Acad. Sci. U.S.A.* **117**, 25700–25711 (2020).
57. J. L. Crowe *et al.*, DNA-PKcs phosphorylation at the T2609 cluster alters the repair pathway choice during immunoglobulin class switch recombination. *Proc. Natl. Acad. Sci. U.S.A.* **117**, 22953–22961 (2020).
58. L. F. Povirk, R. Z. Zhou, D. A. Ramsden, S. P. Lees-Miller, K. Valerie, Phosphorylation in the serine/threonine 2609–2647 cluster promotes but is not essential for DNA-dependent protein kinase-mediated nonhomologous end joining in human whole-cell extracts. *Nucleic Acids Res.* **35**, 3869–3878 (2007).
59. Q. Ding *et al.*, Autophosphorylation of the catalytic subunit of the DNA-dependent protein kinase is required for efficient end processing during DNA double-strand break repair. *Mol. Cell Biol.* **23**, 5836–5848 (2003).
60. K. Meek, V. Dang, S. P. Lees-Miller, DNA-PK: The means to justify the ends? *Adv. Immunol.* **99**, 33–58 (2008).
61. D. W. Chan *et al.*, Autophosphorylation of the DNA-dependent protein kinase catalytic subunit is required for rejoining of DNA double-strand breaks. *Genes. Dev.* **16**, 2333–2338 (2002).
62. A. A. Goodarzi *et al.*, DNA-PK autophosphorylation facilitates Artemis endonuclease activity. *EMBO J.* **25**, 3880–3889 (2006).
63. X. Cui *et al.*, Autophosphorylation of DNA-dependent protein kinase regulates DNA end processing and may also alter double-strand break repair pathway choice. *Mol. Cell Biol.* **25**, 10842–10852 (2005).
64. H. Nagasawa *et al.*, Differential role of DNA-PKcs phosphorylations and kinase activity in radiosensitivity and chromosomal instability. *Radiat Res.* **175**, 83–89 (2010).
65. K. Meek, P. Douglas, X. Cui, Q. Ding, S. P. Lees-Miller, Trans autophosphorylation at DNA-dependent protein kinase's two major autophosphorylation site clusters facilitates end processing but not end joining. *Mol. Cell Biol.* **27**, 3881–3890 (2007).
66. Y. Gao *et al.*, A targeted DNA-PKcs-null mutation reveals DNA-PK-independent functions for KU in V(D)J recombination. *Immunity* **9**, 367–376 (1998).
67. G. E. Taccioli *et al.*, Targeted disruption of the catalytic subunit of the DNA-PK gene in mice confers severe combined immunodeficiency and radiosensitivity. *Immunity* **9**, 355–366 (1998).
68. L. Liu *et al.*, Autophosphorylation transforms DNA-PK from protecting to processing DNA ends. *Mol. Cell* **82**, 177–189.e174 (2022).
69. X. Chen *et al.*, Structure of an activated DNA-PK and its implications for NHEJ. *Mol. Cell* **81**, 801–810.e803 (2021).
70. M. Shrivastav *et al.*, DNA-PKcs and ATM co-regulate DNA double-strand break repair. *DNA Repair (Amst)* **8**, 920–929 (2009).
71. H. Yajima, K. J. Lee, B. P. Chen, ATR-dependent phosphorylation of DNA-dependent protein kinase catalytic subunit in response to UV-induced replication stress. *Mol. Cell Biol.* **26**, 7520–7528 (2006).
72. T. G. W. Graham, S. M. Carney, J. C. Walter, J. J. Loparo, A single XLF dimer bridges DNA ends during nonhomologous end joining. *Nat. Struct. Mol. Biol.* **25**, 877–884 (2018).
73. M. Xing *et al.*, Interactome analysis identifies a new paralogue of XRCC4 in non-homologous end joining DNA repair pathway. *Nat. Commun.* **6**, 6233 (2015).
74. G. J. Grundy *et al.*, The Ku-binding motif is a conserved module for recruitment and stimulation of non-homologous end-joining proteins. *Nat. Commun.* **7**, 11242 (2016).
75. A. K. Chaplin *et al.*, Dimers of DNA-PK create a stage for DNA double-strand break repair. *Nat. Struct. Mol. Biol.* **28**, 13–19 (2021), 10.1038/s41594-020-00517-x.
76. J. Cottarel *et al.*, A noncatalytic function of the ligation complex during nonhomologous end joining. *J. Cell Biol.* **200**, 173–186 (2013).
77. S. Roy *et al.*, XRCC4/XLF interaction is variably required for DNA repair and is not required for ligase IV stimulation. *Mol. Cell Biol.* **35**, 3017–3028 (2015).
78. G. Li *et al.*, Lymphocyte-specific compensation for XLF/cernunnos end-joining functions in V(D)J recombination. *Mol. Cell* **31**, 631–640 (2008).
79. A. Strasser *et al.*, Enforced BCL2 expression in B-lymphoid cells prolongs antibody responses and elicits autoimmune disease. *Proc. Natl. Acad. Sci. U.S.A.* **88**, 8661–8665 (1991).
80. M. Koulnis *et al.*, Identification and analysis of mouse erythroid progenitors using the CD71/TER119 flow-cytometric assay. *J. Vis. Exp.* **54**, 2809 (2011), 10.3791/2809.
81. J. L. Crowe *et al.*, Kinase-dependent structural role of DNA-PKcs during immunoglobulin class switch recombination. *Proc. Natl. Acad. Sci. U.S.A.* **115**, 8615–8620 (2018).
82. Y. Zhu, B. J. Lee, S. Zha, Phosphorylation of DNA-PKcs at the S2056 cluster ensures efficient and productive lymphocyte development in XLF-deficient mice. NCBI Gene Expression Omnibus. https://www.ncbi.nlm.nih.gov/geo/query/acc.cgi?acc=GSE228850. Deposited 3 April 2023.
83. G. G. Faust, I. M. Hall, YAHA: Fast and flexible long-read alignment with optimal breakpoint detection. *Bioinformatics* **28**, 2417–2424 (2012).